Inorganic Chemistry

Article

pubs.acs.org/IC

Syntheses, Structures, and Physical Properties of $CsRE_2Ag_3Te_5$ (RE = Pr, Nd, Sm, Gd−Er) and $RbRE_2Ag_3Te_5$ (RE = Sm, Gd−Dy)

Chang-Yu Meng,*[†,‡] Hong Chen,[†] and Peng Wang[†]

[†]Key Laboratory of Optoelectronic Materials Chemistry and Physics, Fujian Institute of Research on the Structure of Matter, Chinese Academy of Sciences, Fuzhou, Fujian 350002, People's Republic of China

[‡]Department of Chemistry and Materials, Yulin Normal University, Yulin, Guangxi 537000, People's Republic of China

Supporting Information

ABSTRACT: A new series of quaternary $CsRE_2Ag_3Te_5$ (RE = Pr, Nd, Sm, Gd−Er) and $RbRE_2Ag_3Te_5$ (RE = Sm, Gd−Dy), which have been synthesized from the elemental mixtures in ACl flux (A = Rb, Cs) and crystallized in the orthorhombic space group *Cmcm*, with a = 4.620(2)−4.504(2) Å, b = 16.232(8)−16.027(8) Å, c = 18.84(1)−18.32(2) and Z = 4, are isostructural to $RbSm_2Ag_3Se_5$. These isostructural $ARE_2Ag_3Te_5$ feature a three-dimensional tunnel framework constructed by ionically bound $RETe_6$ octahedron and covalently bound $AgTe_4$ tetrahedron in which tunnels are filled by A. Typical semiconducting behavior is revealed by the electrical conductivity, Seebeck coefficient, optical band gap measurement, and the theoretical calculations. The undoped sintered polycrystalline pellets of $CsRE_2Ag_3Te_5$ (containing 1.1−1.7% CsCl impurity) show very low electrical conductivity ($\sigma_{r.t.}$ = 0.5−2.4 S/cm), very low thermal conductivity ($k_{r,t}$ = 0.66−0.53 W/(m·K)), and moderate Seebeck coefficient (160−200 μV/K at 700 K).

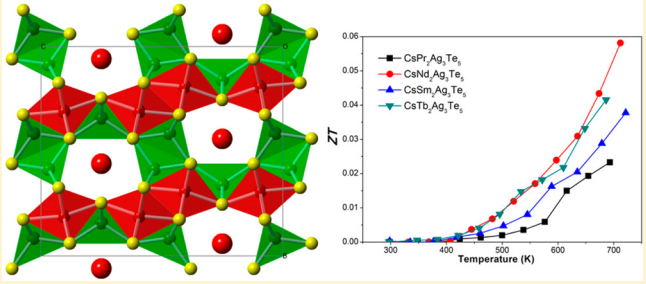

INTRODUCTION

Thermoelectric (TE) materials, which are utilized to convert a temperature gradient into electricity or to convert electricity into a temperature gradient, are a class of functional materials. The current challenge in the efforts for identifying promising TE materials lies in achieving simultaneously high electrical conductivity (σ), high Seebeck coefficient (S), and low thermal conductivity (κ) in the same solid according to the dimensionless figure of merit ZT = $S^2\sigma T/\kappa$,[1] where T is absolute temperature. These parameters are determined by the details of the electronic structure and scattering of charge carriers (electrons or holes) and thus are interdependent, as changing one alters the other, making optimization extremely difficult.[1] Over the past decade, a class of complex structure compounds such as filled skutterudites,[2−4] $CsBi_4Te_6$,[5] $Ba_8Ga_{16}Ge_{30}$,[6] and $AeZn_2Sb_2$[7] (Ae = Sr, Ca, Eu, Yb) have been explored, and it was found that promising TE performances could be obtained. These compounds are all semiconductors whose structures contain a covalently bound substructure region (such as 3D structures $[Co_4Sb_{12}]$ and $[Ga_{16}Ge_{30}]$, and 2D layered structures $[Bi_4Te_6]$ and $[Zn_2Sb_2]$) and an ionic cation substructure region (such as isolated filler RE^{3+}/Ba^{2+}, sheets of Cs^{1+}, and Ae^{2+} cations).[8−10]

Structurally, quaternary alkali- or alkaline-earth/rare earth/Cu(Ag)/Te (A/RE/Cu(Ag)/Te) compounds were similar to the above-mentioned compounds, containing a covalently bound substructure region and a ionic cation substructure region. In A/RE/Cu(Ag)/Te system, with the increase of Cu/(A + RE) atom ratio, the covalently bound $Cu(Ag)Te_4$ tetrahedron can form 1D chains (such as $BaDyCuTe_3$,[11] $CsSc_3Cu_2Te_6$,[12] and $CsGd_2CuTe_4$[13]), 2D layered structure (such as $CsDyCu_3Te_4$,[14a] $KCeCuTe_4$,[14b] $KEuCu_2Te_4$,[15] and $Rb_2CeCu_3Te_5$[16]), and 3D tunnel structure (such as $K_{0.5}Ba_{0.5}DyCu_{1.5}Te_3$,[11] $K_2CeAg_3Te_4$,[17] and $A_xRE_2Cu_{6-x}Te_6$[18]) by sharing-vertex or sharing-edge. $A_xRE_2Cu_{6-x}Te_6$ compounds, whose structure is analogous to that in filled skutterudites containing 3D covalently bound substructure, exhibited relatively high electrical conductivity (477−773 S/cm) at room temperature while maintaining relatively low thermal conductivity (1.42−1.66 W/(m·K)) and obtaining maximum ZT values (0.26, 0.17, and 0.23 at 614, 660, and 660 K for La-, Ce-, and Pr-samples, respectively).[18] The reported A/RE/Cu(Ag)/Te compounds with 2D covalently bound $CuTe_4$ tetrahedral structure, except $CsDyCu_3Te_4$,[14a] either contain the covalently bound square Te nets such as $KCeCuTe_4$[14b] and $KEuCu_2Te_4$[15] or the $[Te-Te]^{2-}$ covalent bonds such as $Rb_2CeCu_3Te_5$.[16] These Te−Te covalent bonds can determine or influence the physical properties. No A/RE/Ag/Te compounds containing only 2D covalently bound $AgTe_4$ tetrahedral structure have been reported to date.

In this Article , we discover new $ARE_2Ag_3Te_5$ compounds, whose structures are similar to $AeZn_2Sb_2$,[7] with sheets of mixed A^{1+} and RE^{3+} cations between layers of covalently bound Ag−

Received: March 26, 2014
Published: June 20, 2014

   dx.doi.org/10.1021/ic5007132 | *Inorg. Chem.* 2014, 53, 6893−6903

Te. Considered as a Zintl phase, $ARE_2Ag_3Te_5$ may be regarded as composed of tetrahedral $[Ag_3Te_5]$ layers separated by $[ARE_2Te_5]$ layers constituted by $RETe_6$ octahedron and ATe_8 polyhedron, with the oxidation states of +1, +3, +1, and −2 for A, RE, Ag, and Te, respectively. In comparison with $A_xRE_2Cu_{6-x}Te_6$ (equivalent to $ARE_2Cu_5Te_6$),[18] $ARE_2Ag_3Te_5$ is used to imagine that a dense $_\infty^3[Cu(Ag)_5Te_6]$ framework is dismantled into a $_\infty^2[Cu(Ag)_3Te_5]$ framework by the elimination of $Cu(Ag)_2Te$, which can be written as

$$ARE_2[Cu(Ag)_5Te_6] - Cu(Ag)_2Te \rightarrow ARE_2[Cu(Ag)_3Te_5] \quad (1)$$

The dimensional reduction leads to an increase of the energy band gaps from 0.09 eV (calculated) of $CsLa_2Cu_5Te_6$ to 0.90 eV (optical)/1.0 eV (calculated) of $CsNd_2Ag_3Te_5$ as orbital overlap in certain space directions is reduced and energy band widths narrow.[19] The primary measurements on undoped sintered polycrystalline pellets of $CsRE_2Ag_3Te_5$ (with 1.2, 1.1, 1.3, and 1.7% CsCl impurity for Pr-, Nd-, Sm-, and Tb-samples, respectively) show very low electrical conductivity ($\sigma_{r.t.}$ = 0.5−2.4 S/cm), very low thermal conductivity ($k_{r,t}$ = 0.66−0.53 W/(m·K)) and moderate Seebeck coefficient (160−200 μV/K at 700 K). Owing to the very low electrical conductivity, the values of ZT are too low for practical applications as thermoelectric materials, with 0.02 at 693 K, 0.06 at 712 K, 0.04 at 721 K, and 0.04 at 686 K, for undoped Pr-, Nd-, Sm-, and Tb-samples, respectively.

This Article details the syntheses, structures, and physical properties measurements as well as band structure studies of $ARE_2Ag_3Te_5$.

EXPERIMENTAL SECTION

Syntheses. The following reactants were used as-purchased and stored in a glovebox filled with purified Ar (moisture and oxygen level >0.1 ppm), and all manipulations were performed inside the glovebox. Rare earth elements were purchased from Huhhot Jinrui Rare Earth Co., Ltd. Pr (99.95%), Nd (99.95%), Sm (99.95%), Gd (99.95%), Tb (99.95%), Dy (99.95%), Ho (99.95%), Er (99.95%), Ag (99.9%, 200−300 mesh), and Te (99.99%) were purchased from Alfa Aesar China (Tianjin) Co., Ltd. RbCl (99.9%) and CsCl (99.9%) were purchased from XinJiang Research Institute of Non-Ferrous Metals.

The $ARE_2Ag_3Te_5$ compounds were synthesized by mixing 2.4 mmol of RE, 5 mmol of Te, 3 mmol of Ag, and 3 mmol of ACl via the high-temperature solid-state reaction. ACl worked as a flux to assist the crystallization of the target compounds and as a Cs source in these reactions. A reaction mixture was loaded into a fused-silica tube under an Ar atmosphere in a glovebox. The tube was sealed under a 10^{-3} Pa atmosphere and then placed in a temperature-controlled furnace. The sample was heated at 75 K/h to 673 K and then to 1123 K at 10 K/h, at which it remained for 100 h. The mixture was then slowly cooled to 873 at 2 K/h, and finally cooled to 300 K within 10 h. The raw products were washed first with distilled water three times to remove excess flux and the chloride byproducts, and then it was dried with ethanol. After the washing step, the title compounds were subjected to X-ray diffraction (XRD) to identify the pure target compounds (Figure 1; Figures S2−S13, Supporting Information). All the title compounds crystallized as gray blocks or chunks and were stable in air at room temperature for one year.

Synthesis of the Ingot for Thermoelectric Property Measurement. The mixture of 21 mmol of CsCl, 24 mmol of RE, 30 mmol of Ag, and 50 mmol of Te was placed in a silica tube (11 × 13 mm). The silica tube was then evacuated, sealed, and placed perpendicularly inside a temperature-controlled furnace. The sample was heated at 75 K/h to 873 K, then at 10 K/h to 1123 K, where it remained for 100 h, then at 5 K/h to 1223 K, where it remained for 10 h, and then cooled at 5 K/h to 873 K, at which point the power to the furnace was turned off. This process generated an ingot of $CsRE_2Ag_3Te_5$ inside the silica jacket. A series of XRD analyses on the ingot showed that the bottom of the ingot (about 4−5 mm in thickness) was mostly the title compound (Figure 2), while the supper part of the ingot was mainly a eutectic mixture of CsCl and Cs_3RECl_6.[18,20−24] The amount of CsCl was detected by chlorine titration. For different batches of bottom samples, the chloride ion concentration was about 1.1−1.7 wt % of CsCl (Supporting Information), which is beyond the limits of XRD detection. The thermal diffusivity and heat capacity were measured on a disk (diameter, ∼11 mm; thickness, ∼4 mm), cut from the bottom part of the ingot, and further polished with sandpaper into a size of ∼10 mm in diameter and ∼3 mm in thickness without washing. The measured density of the pellet was ∼95% of the theoretical density. Subsequently, the disk was cut into a rectangular bar (∼9 × 3 × 2 mm^3) on which the Seebeck coefficient and electrical conductivity were measured. After three runs of the heating and cooling treatment on the pellet during the measurement, the XRD analyses did not show changes in either the phase identity or the percentage of each phase (Figure 2).

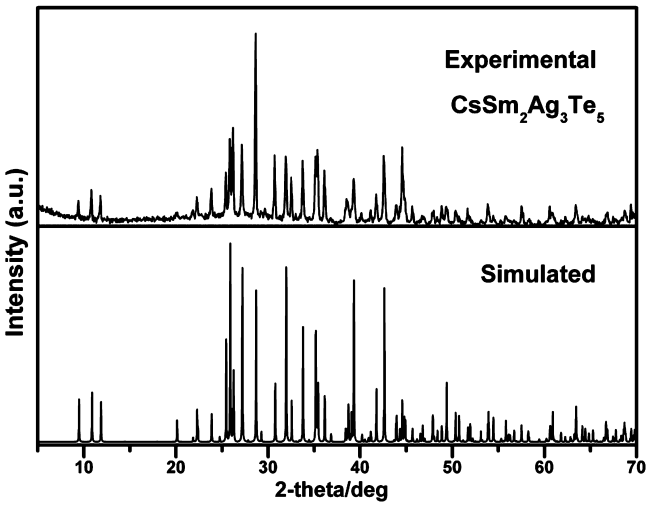

Figure 1. (Top) Experimental and (bottom) simulated XRD patterns for $CsSm_2Ag_3Te_5$.

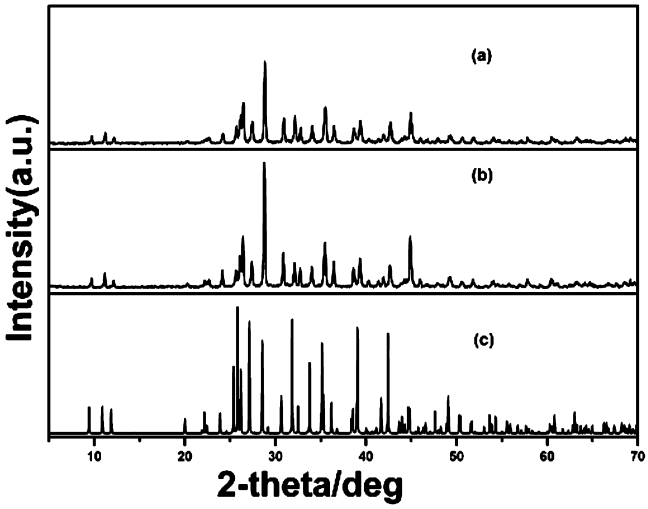

Figure 2. XRD patterns taken on the bottom part of a sintered ingot (a) before and (b) after thermoelectric property measurements and (c) simulated XRD pattern of $CsNd_2Ag_3Te_5$.

Crystal Structure Determinations. The single-crystal XRD data were collected on a Rigaku SCXmini CCD diffractometer equipped

dx.doi.org/10.1021/ic5007132 | Inorg. Chem. 2014, 53, 6893−6903

Table 1. Crystallographic Data for $CsRE_2Ag_3Te_5$ (RE = Pr, Nd, Sm, Gd−Er) and $RbRE_2Ag_3Te_5$ (RE = Sm, Gd−Dy)[a]

	$CsPr_2Ag_3Te_5$	$CsNd_2Ag_3Te_5$	$CsSm_2Ag_3Te_5$	$CsGd_2Ag_3Te_5$
fw	1376.33	1382.99	1395.23	1409.01
a (Å)	4.620(2)	4.609(3)	4.5795(6)	4.552(3)
b (Å)	16.232(8)	16.217(9)	16.251(2)	16.260(2)
c (Å)	18.840(1)	18.750(2)	18.648(2)	18.550(2)
V (Å^3)	1413(2)	1401(2)	1387.9(3)	1373.0(2)
D_c (g cm^{-3})	6.472	6.555	6.677	6.819
μ (mm^{-1})	23.463	24.107	25.322	26.712
$R1$, $wR2$ ($I > 2\sigma(I)$)	0.0282, 0.0699	0.0200, 0.0342	0.0208, 0.0410	0.0243, 0.0492
$R1$, $wR2$ (all data)	0.0289, 0.0703	0.0211, 0.0344	0.0235, 0.0418	0.0282, 0.0754
	$CsTb_2Ag_3Te_5$	$CsDy_2Ag_3Te_5$	$CsHo_2Ag_3Te_5$	$CsEr_2Ag_3Te_5$
fw	1412.36	1419.51	1424.37	1429.03
a (Å)	4.5415(6)	4.523(3)	4.5226(10)	4.504(2)
b (Å)	16.304(3)	16.290(2)	16.299(3)	16.316(8)
c (Å)	18.502(2)	18.470(2)	18.455(4)	18.410(1)
V (Å^3)	1370(3)	1361(2)	1360.4(5)	1353.0(2)
D_c (g/cm^3)	6.848	6.930	6.955	7.017
μ (mm^{-1})	27.405	28.182	28.833	29.705
$R1$, $wR2$ ($I > 2\sigma(I)$)[b]	0.0191, 0.0350	0.0303, 0.0651	0.0280, 0.0516	0.0231, 0.0495
$R1$, $wR2$ (all data)	0.0210, 0.0356	0.0345, 0.0668	0.0344, 0.0534	0.0272, 0.0514
	$RbSm_2Ag_3Te_5$	$RbGd_2Ag_3Te_5$	$RbTb_2Ag_3Te_5$	$RbDy_2Ag_3Te_5$
fw	1347.79	1361.57	1364.92	1372.07
a (Å)	4.568(2)	4.548(3)	4.529(3)	4.5324(8)
b (Å)	16.027(8)	16.06(2)	16.06(2)	16.102(2)
c (Å)	18.453(9)	18.42(2)	18.32(2)	18.324(3)
V (Å^3)	1351(2)	1345(2)	1333(2)	1337(1)
D_c (g/cm3)	6.627	6.723	6.804	6.815
μ (mm^{-1})	26.940	28.183	29.113	29.606
$R1$, $wR2$ ($I > 2\sigma(I)$)	0.0229, 0.0602	0.0236, 0.0558	0.0269, 0.0618	0.0290, 0.0489
$R1$, wR_2 (all data)	0.0234, 0.0605	0.0251, 0.0566	0.0305, 0.0636	0.0333, 0.0501

[a]For all structures, $Z = 4$, space group = $Cmcm$, $T = 293(2)$ K, and $\lambda = 0.71073$ Å. [b]$R1 = \sum||F_0|-|F_c||/\sum|F_0|$, $_wR2 = [\sum w(F_0^2-F_c^2)^2/\sum w(F_0^2)^2]^{1/2}$.

with a graphite-monochromated Mo Kα radiation source ($\lambda = 0.71073$ Å) at 293 K. The absorption corrections were done by the multiscan method.[25] Their lattice types and space groups were suggested by the systematic absence conditions of the collected data. All structures were solved by the direct methods and refined by the full-matrix least-squares fitting on F^2 in the $Cmcm$ space group by SHELX-97.[26] The assignments of A, RE, Ag, and Te were determined on the basis of the interatomic distances and relative displacement parameters. All of the atoms were refined with anisotropic thermal parameters and a secondary extinction correction. The program PLATON was used to check the final refined crystal structures of $ARE_2Ag_3Te_5$.

Table 1 summarizes the crystallographic data and structural refinement details, the positional coordinates and anisotropic parameters are given in Table 2, and some important bond distances are listed in Table3. More details of the crystallographic data are given in Table S1 (Supporting Information).

Elemental Analyses. Microprobe elemental analyses were performed on several single crystals of the $ARE_2Ag_3Te_5$ compounds, including the crystals used for X-ray diffraction analysis. Spectra were collected on a field emission scanning electron microscope (FESEM, JSM6700F) equipped with an energy dispersive X-ray spectroscope (EDX, Oxford INCA). As an example, the EDX results for $CsPr_2Ag_3Te_5$ indicated the presence of the elements Cs, Pr, Ag, and Te, and no Cl from the flux, Si, or O from the quartz tube was detected in any case. The EDX analyses gave an average atomic composition (atomic %) of 8.4(1) % Cs, 17.2(2) % Pr, 29.2(1) % Ag, and 45.1(1) % Te that generates Cs/Pr/Ag/Te = 0.93:1.85:3.24:5, which is in good agreement with the composition obtained from the single crystal refinement of $CsPr_2Ag_3Te_5$.

An Ultima-2 inductively coupled plasma emission spectrometer (ICP-OES) was used to quantitatively determine the composition of the bottom parts of the corresponding sintered ingots. The result of ICP measurement indicated that the RE/Ag/Te ratios were $Pr_{1.88}Ag_{3.04}Te_5$, $Nd_{1.87}Ag_{3.01}Te_5$, $Sm_{1.90}Ag_{3.16}Te_5$, and $Tb_{1.87}Ag_{3.14}Te_5$, which suggested that the bottom parts did not contain significant impurities. The chloride ion concentration of the bottom parts of the sintered ingot had been measured by Volhard's Method titration (Support Information). One gram of each of sample contained about 0.07, 0.06, 0.08, and 0.10 mmol of Cl^-, which are equivalent to 0.012, 0.011, 0.013, and 0.017g of CsCl, for Pr-, Nd-, Sm-, and Tb-sampless, respectively.

X-ray Powder Diffraction. The powder XRD patterns were taken at room temperature on a Rigaku DMAX 2500 powder diffractometer or Rigaku MiniFlex II powder diffractometer with monochromatized Cu Kα radiation. Data were collected at a scanning rate of 5°/min over 2θ, ranging from 5 to 70°.

UV−Vis Diffuse Reflectance Spectroscopy. The optical diffuse reflectance spectrum of $CsRE_2Ag_3Te_5$ powder was measured at room temperature using a PerkinElmer Lambda 900 UV−vis spectrophotometer equipped with an integrating sphere attachment and $BaSO_4$ as a reference. The absorption spectrum was calculated from the reflection spectrum via the Kubelka−Munk function: $\alpha/S = (1-R)^2/2R$, in which α is the absorption coefficient, S is the scattering coefficient, and R is the reflectance.[27]

Magnetic Susceptibility Measurements. The direct current (dc) magnetic susceptibility measurements were performed on a Quantum Design MPMS-XL magnetometer for the $ARE_2Ag_3Te_5$ in the temperature range of 2−300 K. The X-ray pure polycrystalline samples were ground to fine powders to minimize the possible anisotropic effects and loaded into a gelatin capsule. The data were corrected for the susceptibility of the container and for the diamagnetic contribution from the ion core.

Electronic Structure Calculations. The electronic band structure calculations of the compounds $CsRE_2Ag_3Te_5$ (RE = Pr, Nd) were

dx.doi.org/10.1021/ic5007132 | Inorg. Chem. 2014, 53, 6893−6903

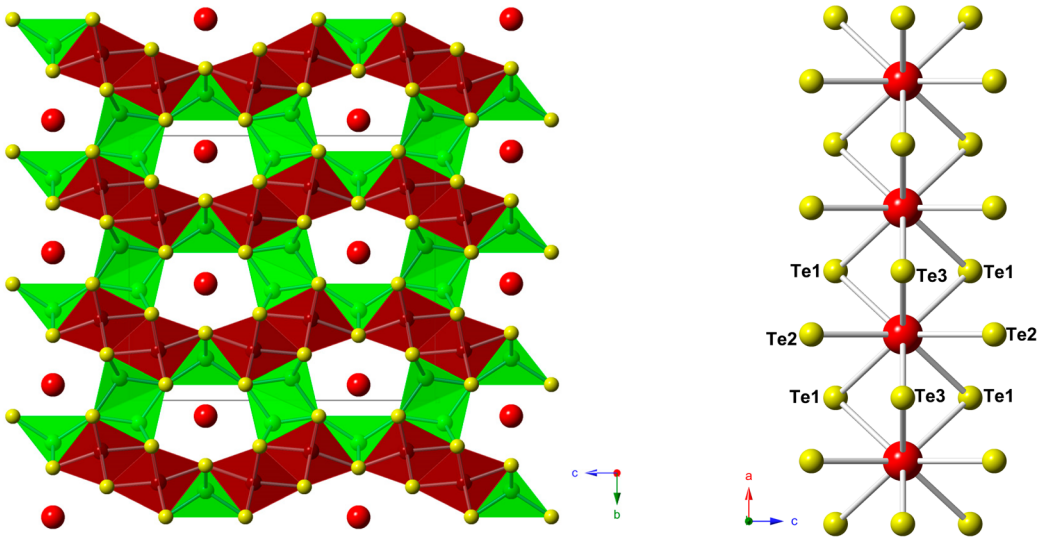

Figure 3. Crystal structures of $CsNd_2Ag_3Te_5$ (left) viewed along [100] and 1D chain of $^1_\infty[CsTe_5]$ and (right) viewed along the *a* axis for $CsNd_2Ag_3Te_5$. Green: Ag. Yellow: Te. Red: Cs. Dark red: Nd.

performed by the Vienna ab initio simulation package VASP.[28] The generalized gradient approximation (GGA)[29] was chosen as the exchange−correlation functional, and a plane wave basis with the projector augmented wave (PAW) potential was used.[30,31] The plane-wave cutoff energy of 400 eV and the total electronic energy threshold of 10^{-6} eV were set for the self-consistent-field (SCF) convergence target. A total of 72 irreducible k-points in the IBZ were used during SCF. The 4f electrons of RE were treated as core electrons, and the valence electrons of other elements included Cs, $5s^25p^66s^1$; Ag, $4d^{10}5s^1$; and Te, $5s^25p^4$.

Thermoelectric Property Measurements. The thermal diffusivity and heat capacity of $CsRE_2Ag_3Te_5$ were measured by laser flash techniques with a Netzsch LFA 457 system in an Ar atmosphere with pyroceram 9606 as the standard for heat capacity measurement. The thermal conductivity was calculated according to the equation $\kappa(T) = \alpha(T)\ C_p(T)\rho(T)$, in which $\rho(T)$ is the experimental density, $C_p(T)$ is the heat capacity, and $\alpha(T)$ is the measured thermal diffusivity. The Seebeck coefficient and electrical conductivity of a rectangular bar (~9 3 × 2 mm^3) cut from the above-mentioned disk were measured on a ULVAC ZEM-3 instrument from room temperature to about 700 K. Each curve was measured three times in the temperature range to ensure the stability and repeatability of the data.

RESULTS AND DISCUSSION

Syntheses. Analogous to the synthesis of $A_xRE_2Cu_{6-x}Te_6$,[18] considering the charge-balanced formula $ARE_2Ag_3Te_5$ of the title compounds, the reactions may be expressed by eq 2. In powdery samples, the byproducts A_3RECl_6 and ACl will react with water and thus can be washed out. As with the $A_xRE_2Cu_{6-x}Te_6$, the hot-press technique cannot make a dense pellet from such pure powders (suffering with low density and spallation). Thus, a direct sintering route on a large scale with a total loading weight of about 17 g has to develop to produce a highly compact ingot. As discussed above, the bottom part of the ingot is the title compound together with enwrapped minor CsCl impurity (1.1−1.7%) which is beyond the detection range of XRD. As previously discussed, in $A_xRE_2Cu_{6-x}Te_6$,[18] the drawback of such a route is that CsCl imbedded inside the ingot cannot be washed out by immergence without grinding, and such a direct sintering method is the best approach at present to produce pellets exhibiting properties that are the closest to the intrinsic TE properties of the title compounds.

$$2.4RE + 3Ag + 5Te + 3ACl\ (excess) \xrightarrow{1123\ K} ARE_2Ag_3Te_5 + 0.4A_3RECl_6 + 0.8ACl \quad (2)$$

Crystal Structures. The compounds $CsRE_2Ag_3Te_5$ (RE = Pr, Nd, Sm, Gd−Er) and $RbRE_2Ag_3Te_5$ (RE = Sm, Gd−Dy), crystallizing in the orthorhombic space group *Cmcm* with *a* = 4.620(2)−4.504(2) Å, *b* = 16.232(8)−16.027(8) Å, *c* = 18.84(1)−18.41(1), and *Z* = 4 on going from RE = Pr, Nd, Sm, Gd to Er, A = Cs to Rb (details are listed in Table1), are isostructural to $RbSm_2Ag_3Se_5$.[32] The decrease of the unit cell volume reflects the lanthanide contraction and size effect of A^+.

For simplicity, the structure of $CsNd_2Ag_3Te_5$ will be discussed in detail as a representative, and the structure of $CsNd_2Ag_3Te_5$ is illustrated in Figure 3 (left). These isostructural $ARE_2Ag_3Te_5$ compounds feature a three-dimensional tunnel structure constructed by covalently bound $AgTe_4$ tetrahedron and ionically bound $RETe_6$ octahedron, and whose tunnels are filled by A cations. There are two crystallographically distinct Ag sites (Ag1, site symmetry *m*2*m*; Ag2, site symmetry *m*) that form two different types of chains in the Ag sublattice of $ARE_2Ag_3Te_5$. Ag1 atom is coordinated in a distorted $Ag1Te_4$ tetrahedron with Ag1−Te (×2) and Ag1−Te (×2) distance (Table 2) of 2.772(2) and 2.923(2) Å, whereas Ag2 atom is coordinated in a slightly distorted $Ag2Te_4$ tetrahedron with Ag2−Te (×1), Ag2−Te (×1) and Ag2−Te (×2) distance of 2.850(2), 2.891(2), and 2.824(2) Å (Table 2) for $CsNd_2Ag_3Te_5$ as an example. Each $Ag1Te_4$ tetrahedron shares two neighboring vertex (Te3) with two other $Ag1Te_4$ tetrahedron forming a $^1_\infty[AgTe_3]$ single chain, whereas the $Ag2Te_4$ tetrahedron forms $^1_\infty[Ag_2Te_4]$ double chains by vertex (Te2)- and edge (Te1−Te1)-sharing along the *a* axis. The $^1_\infty[AgTe_3]$ single chain and $^1_\infty[Ag_2Te_4]$ double chains further link to each other by vertices (Te1)-sharing to form the covalently bound "puckered" layers of $^2_\infty[Ag_3Te_5]$ along the *c* axis (Figure 4, left). The $RETe_6$ octahedron is slightly distorted (Table 2). The $RETe_6$ octahedron propagates down the *a* axis as a double-octahedron-chain via sharing two neighboring edges. These $^1_\infty[RE_2Te_6]$ double chains link to each other by vertices(Te3)-sharing to form the ionically bound "puckered" layers of $^2_\infty[RE_2Te_5]$ along the *c* axis (Figure 4, right). The

dx.doi.org/10.1021/ic5007132 | Inorg. Chem. 2014, 53, 6893−6903

Table 2. Atomic Coordinates ($\times 10^{-4}$) and Equivalent Isotropic Displacement Parameters ($Å^2 \times 10^{-3}$) for $CsRE_2Ag_3Te_5$ (RE = Pr, Nd, Sm, Gd−Er) and $RbRE_2Ag_3Te_5$ (RE = Sm, Gd−Dy)

atom	Wyckoff	x	y	z	U(eq)[a]
			$CsPr_2Ag_3Te_5$		
Cs	4c	0	4406(1)	2500	22(1)
Pr	8f	0	3092(1)	5937(1)	14(1)
Te1	8f	0	9403(1)	6197(1)	15(1)
Te2	8f	0	3271(1)	729(1)	14(1)
Te3	4f	0	7538(1)	2500	16(1)
Ag1	4c	0	1592(1)	2500	27(1)
Ag2	8f	0	9143(1)	304(1)	24(1)
			$CsNd_2Ag_3Te_5$		
Cs	4c	0	4408(1)	2500	21(1)
Nd	8f	0	3091(1)	5937(1)	13(1)
Te1	8f	0	9397(1)	6195(1)	14(1)
Te2	8f	0	3263(1)	729(1)	13(1)
Te3	4f	0	7540(1)	2500	15(1)
Ag1	4c	0	1590(1)	2500	26(1)
Ag2	8f	0	9144(1)	309(1)	23(1)
			$CsSm_2Ag_3Te_5$		
Cs	4c	0	4412(1)	2500	22(1)
Sm	8f	0	3089(1)	5939(1)	14(1)
Te1	8f	0	9383(1)	6191(1)	15(1)
Te2	8f	0	3247(1)	727(1)	13(1)
Te3	4f	0	7541(1)	2500	15(1)
Ag1	4c	0	1586(1)	2500	26(1)
Ag2	8f	0	9152(1)	324(1)	24(1)
			$CsGd_2Ag_3Te_5$		
Cs	4c	0	4415(1)	2500	21(1)
Gd	8f	0	3085(1)	5940(1)	14(1)
Te1	8f	0	9371(1)	6188(1)	14(1)
Te2	8f	0	3237(1)	724(1)	13(1)
Te3	4f	0	7547(1)	2500	15(1)
Ag1	4c	0	1586(1)	2500	25(1)
Ag2	8f	0	9161(1)	335(1)	24(1)
			$CsTb_2Ag_3Te_5$		
Cs	4c	0	4420(1)	2500	21(1)
Tb	8f	0	3081(1)	5941(1)	13(1)
Te1	8f	0	9361(1)	6185(1)	14(1)
Te2	8f	0	3231(1)	719(1)	12(1)
Te3	4f	0	7548(1)	2500	14(1)
Ag1	4c	0	1585(1)	2500	25(1)
Ag2	8f	0	9167(1)	345(1)	25(1)
			$CsDy_2Ag_3Te_5$		
Cs	4c	0	4424(1)	2500	22(1)
Dy	8f	0	3077(1)	5943(1)	15(1)
Te1	8f	0	9352(1)	6182(1)	15(1)
Te2	8f	0	3227(1)	716(1)	14(1)
Te3	4f	0	7551(1)	2500	16(1)
Ag1	4c	0	1584(1)	2500	27(1)
Ag2	8f	0	9174(1)	354(1)	27(1)

atom	Wyckoff	x	y	z	U(eq)[a]
			$CsHo_2Ag_3Te_5$		
Cs	4c	0	4426(1)	2500	24(1)
Ho	8f	0	3075(1)	5945(1)	16(1)
Te1	8f	0	9344(1)	6181(1)	17(1)
Te2	8f	0	3221(1)	713(1)	15(1)
Te3	4f	0	7555(1)	2500	17(1)
Ag1	4c	0	1586(1)	2500	28(1)
Ag2	8f	0	9180(1)	363(1)	28(1)
			$CsEr_2Ag_3Te_5$		
Cs	4c	0	4430(1)	2500	22(1)
Er	8f	0	3071(1)	5947(1)	15(1)
Te1	8f	0	9334(1)	6178(1)	15(1)
Te2	8f	0	3219(1)	709(1)	13(1)
Te3	4f	0	7559(1)	2500	15(1)
Ag1	4c	0	1588(1)	2500	27(1)
Ag2	8f	0	9187(1)	372(1)	27(1)
			$RbSm_2Ag_3Te_5$		
Rb	4c	0	4418(1)	2500	24(1)
Sm	8f	0	3094(1)	5945(1)	12(1)
Te1	8f	0	9405(1)	6226(1)	14(1)
Te2	8f	0	6737(1)	5734(1)	12(1)
Te3	4f	0	7610(1)	2500	14(1)
Ag1	4c	0	1636(1)	2500	24(1)
Ag2	8f	0	9142(1)	293(1)	22(1)
			$RbGd_2Ag_3Te_5$		
Rb	4c	0	4420(1)	2500	23(1)
Gd	8f	0	3093(1)	5946(1)	12(1)
Te1	8f	0	9395(1)	6223(1)	13(1)
Te2	8f	0	6749(1)	5731(1)	11(1)
Te3	4f	0	7612(1)	2500	13(1)
Ag1	4c	0	1636(1)	2500	23(1)
Ag2	8f	0	9150(1)	303(1)	21(1)
			$RbTb_2Ag_3Te_5$		
Rb	4c	0	4423(1)	2500	27(1)
Tb	8f	0	3091(1)	5947(1)	15(1)
Te1	8f	0	9385(1)	6219(1)	16(1)
Te2	8f	0	6757(1)	5728(1)	14(1)
Te3	4f	0	7612(1)	2500	16(1)
Ag1	4c	0	1635(1)	2500	26(1)
Ag2	8f	0	9155(1)	313(1)	25(1)
			$RbDy_2Ag_3Te_5$		
Rb	4c	0	4425(1)	2500	26(1)
Dy	8f	0	3088(1)	5949(1)	15(1)
Te1	8f	0	9377(1)	6217(1)	15(1)
Te2	8f	0	6763(1)	5724(1)	14(1)
Te3	4f	0	7614(1)	2500	16(1)
Ag1	4c	0	1634(1)	2500	26(1)
Ag2	8f	0	9160(1)	322(1)	25(1)

tunnels are formed when the "puckered" layer of $^2_\infty[Ag_3Te_5]$ alternately stacks with the "puckered" layer of $^2_\infty[RE_2Te_5]$ along the *b* axis (Figure 3, left). Note that these tunnels are totally different from those of $A_xRE_2Cu_{6-x}Te_6$; the latter are constructed by covalently bound $CuTe_4$ tetrahedral. The A cations are coordinated to eight Te atoms in a bicapped trigonal−prismatic arrangement (Figure 3, right) with Cs−Te1 (×4), Cs−Te2 (×2), Cs−Te3 (×2) distances of 3.880(2), 3.805(2), and 3.807(2) Å, respectively, for $CsNd_2Ag_3Te_5$ as an example (Table 2). Each A cation is filled in a 10-membered ring composed of six Cu−Te bonds and four RE−Te bonds. Because there is no Te−Te bond in $CsRE_2Ag_3Te_5$, the formal oxidation states of A, RE, Ag, and Te can be assigned as 1+, 3+, 1+, and 2−, respectively.

Selected bond distances for $ARE_2Ag_3Te_5$ are displayed in Table 3. The RE−Te distances are 3.038(2)−3.223(2) Å. These ranges are consistent with the previously reported distances of 3.0296(7)−3.3585(5) Å in, for example, $CsREZnTe_3$,[33] $CsRECdTe_3$,[34] $RECu_{(0.32-0.40)}Te_2$,[35] and $Rb_2Cu_3CeTe_5$.[16] The RE−Te distances of $ARE_2Ag_3Te_5$ show

dx.doi.org/10.1021/ic5007132 | Inorg. Chem. 2014, 53, 6893−6903

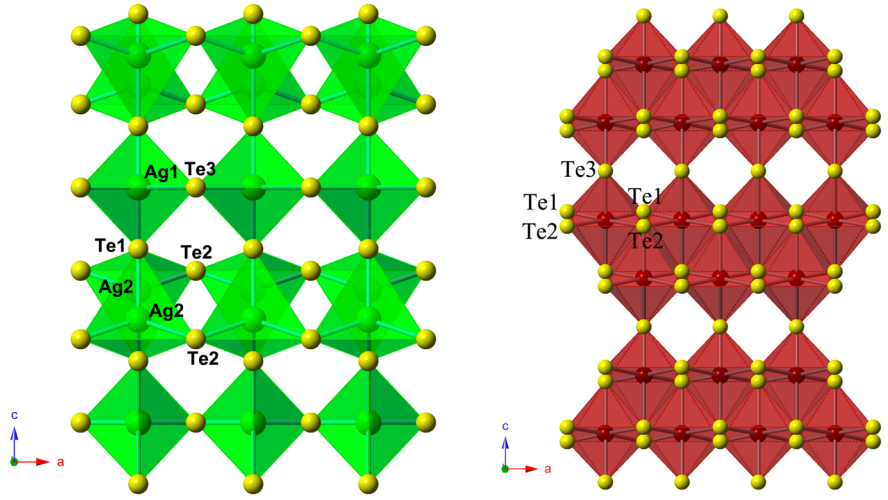

Figure 4. (Left) 2D layer of $^{2}_{\infty}[Ag_3Te_5]$ and (right) 2D layer of $^{2}_{\infty}[Nd_2Te_5]$ viewed along [010] for $CsNd_2Ag_3Te_5$. Green: Ag. Yellow: Te. Dark red: Nd.

Table 3. Selected Bonds Distances (Å) for $CsRE_2Ag_3Te_5$ (RE = Pr, Nd, Sm, Gd−Er) and $RbRE_2Ag_3Te_5$ (RE = Sm, Gd−Dy)

	Cs−Pr	Cs−Nd	Cs−Sm	Cs−Gd	Cs−Tb	Cs−Dy
A−Te1 (×4)	3.885(2)	3.880(2)	3.877(1)	3.872(2)	3.877(1)	3.875(2)
A−Te2 (×2)	3.811(2)	3.805(2)	3.811(1)	3.811(2)	3.822(1)	3.828(3)
A−Te3 (×2)	3.812(2)	3.807(2)	3.806(1)	3.794(3)	3.803(1)	3.797(3)
RE−Te1 (×2)	3.179(2)	3.167(2)	3.145(1)	3.124(2)	3.117(1)	3.101(2)
RE−Te2 (×1)	3.151(2)	3.136(2)	3.116(1)	3.096(2)	3.082(1)	3.073(3)
RE−Te2 (×2)	3.223(2)	3.206(2)	3.180(1)	3.156(2)	3.147(1)	3.132(2)
RE−Te3 (×1)	3.117(2)	3.104(2)	3.087(1)	3.071(2)	3.061(1)	3.053(2)
Ag1−Te1 (×2)	2.937(2)	2.923(2)	2.905(1)	2.888(2)	2.881(1)	2.871(2)
Ag1−Te3 (×2)	2.774(2)	2.772(2)	2.767(1)	2.760(2)	2.762(1)	2.755(2)
Ag2−Te1 (×1)	2.858(2)	2.850(2)	2.850(1)	2.848(3)	2.847(1)	2.848(2)
Ag2−Te1 (×1)	2.899(2)	2.891(2)	2.879(1)	2.862(2)	2.859(1)	2.853(3)
Ag2−Te2 (×2)	2.825(2)	2.824(2)	2.823(1)	2.820(2)	2.823(1)	2.817(2)
	Cs−Ho	Cs−Er	Rb−Sm	Rb−Gd	Rb−Tb	Rb−Dy
A−Te1 (×4)	3.881(1)	3.880(2)	3.782(2)	3.785(2)	3.781(2)	3.793(1)
A−Te2 (×2)	3.838(1)	3.845(2)	3.748(2)	3.760(2)	3.759(2)	3.776(2)
A−Te3 (×2)	3.797(2)	3.794(2)	3.690(2)	3.689(2)	3.686(3)	3.693(2)
RE−Te1 (×2)	3.095(1)	3.083(2)	3.146(2)	3.131(2)	3.114(2)	3.112(1)
RE−Te2 (×1)	3.070(1)	3.057(2)	3.110(2)	3.100(2)	3.079(2)	3.074(1)
RE−Te2 (×2)	3.124(1)	3.113(2)	3.178(2)	3.161(2)	3.143(2)	3.139(1)
RE−Te3 (×1)	3.047(1)	3.038(2)	3.083(2)	3.077(2)	3.060(2)	3.060(1)
Ag1−Te1 (×2)	2.867(1)	2.861(2)	2.884(2)	2.877(2)	2.861(2)	2.860(1)
Ag1−Te3 (×2)	2.758(1)	2.754(2)	2.766(2)	2.762(2)	2.755(2)	2.762(1)
Ag2−Te1 (×1)	2.841(2)	2.833(2)	2.835(2)	2.838(2)	2.831(2)	2.842(2)
Ag2−Te1 (×1)	2.862(2)	2.864(2)	2.896(2)	2.886(2)	2.874(2)	2.870(2)
Ag2−Te2 (×2)	2.824(1)	2.820(2)	2.803(2)	2.806(2)	2.802(2)	2.808(1)

monotonic shrinking with an increase of 4f electrons in the RE^{3+} ion. The Cs−Te distances are 3.794(2)−3.885(2) Å and are in the range of those in $Cs_2Cd_3Te_4$ [3.883(1)−4.003(1) Å],[36] $CsREZnTe_3$ [3.7933(8)−4.2665(6) Å],[33] and $CsRECdTe_3$ [3.810(5)−4.201(2) Å].[34] The Rb−Te distances are 3.686(3)−3.785(2) Å and are in the range of those in $Rb_3Cu_8Te_{10}$ [3.698(6)−4.190(9) Å].[37] The Ag−Te distances are 2.754(2)−2.937(2) Å and are in the range of those in $K_2CeAg_3Te_4$ [2.7781(1)−3.182 (2) Å].[17]

Magnetic Properties. The magnetic susceptibility of $CsRE_2Ag_3Te_5$ (RE = Pr, Nd, Sm, Gd, Tb) was measured over the range 2−300 K at 1000 Oe, and the plots of the reciprocal of the molar susceptibility ($1/\chi_M$) versus T are displayed in Figure 5. The susceptibility data were fit by the least-squares method to the Curie−Weiss equation, $\chi_M = C/(T - \theta)$, where χ_M is the magnetic susceptibility, C is the Curie constant, and θ is the Weiss constant. The effective magnetic moment ($\mu_{eff(total)}$) was calculated from the equation $\mu_{eff(total)} = (7.997C)^{1/2}\ \mu_B$.[38] $CsRE_2Ag_3Te_5$ (RE = Pr, Gd, Tb) obeys the Curie−Weiss law in the entire experimental temperature region, while $CsNd_2Ag_3Te_5$ exhibits nearly Curie−Weiss behavior with only slight deviation from linearity beginning below 50 K. For Pr-, Gd-, and Tb-compounds, the linear fitting of $1/\chi_M$ with T over the whole temperature indicates Curie constants (C) of 3.07, 15.27, and 23.40 $cm^3\ mol^{-1}$ K; Weiss constants (θ) of −37.19, −4.32, and −7.53 K; and effective magnetic moments (μ_{eff}) of 4.96 μ_B, 11.05 μ_B, and 13.68 μ_B, respectively. For the Nd-compound, these values are 3.23 cm^3

dx.doi.org/10.1021/ic5007132 | Inorg. Chem. 2014, 53, 6893−6903

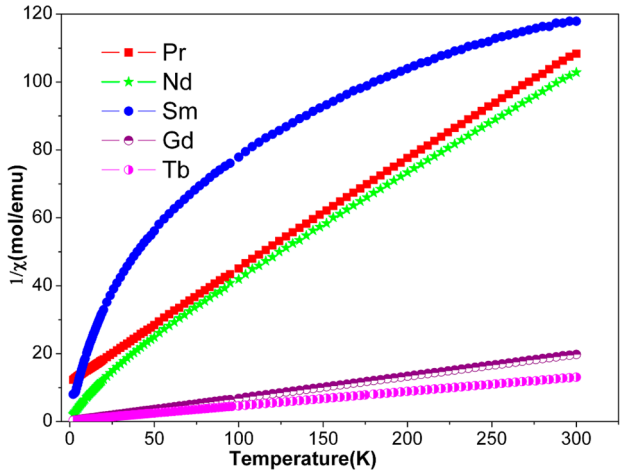

Figure 5. Plots of $1/\chi_M$ vs temperature (T) for $CsRE_2Ag_3Te_5$ (RE = Pr, Nd, Sm, Gd, Tb).

mol^{-1} K, −35.66 K, and 5.08 μ_B, respectively, at temperatures above 50 K. Because there were 2 RE^{3+} ions per formula, the μ_{eff} values were estimated to be 3.51 μ_B per Pr^{3+}, 3.59 μ_B per Nd^{3+}, 7.81 μ_B per Gd^{3+}, and 9.67 μ_B per Tb^{3+}, according to the equation $\mu_{eff} = \mu_{eff(total)}/(2^{1/2})$,[39] which are in agreement with the theoretical values of an isolated magnetic center per formula unit (3.58 μ_B, 3.62 μ_B, 7.94 μ_B, and 9.72 μ_B, respectively).[38] The Sm-compound does not obey the Curie−Weiss law. The distinct magnetic behavior of $CsSm_2Ag_3Te_5$ is typical for Sm^{3+} chalcogenides,[40,41] because the 6H ground term for Sm^{3+} is split as a result of spin−orbit coupling, which leads to a temperature dependence of the effective moment of the 4f electrons.[42]

Optical Properties. The optical band gap of $CsRE_2Ag_3Te_5$ has been measured by the diffuse-reflectance spectra at room temperature, as shown in Figure 6. The optical band gap is estimated to be about 0.90 eV for Nd- and Sm-members. The wider band gap of $CsRE_2Ag_3Te_5$ may result from the stronger ionic interactions between the alkali metal/rare-earth ions and the $[Ag_3Te_5]^{7-}$ framework as well as the dimensional reduction. In general, the band gap of compounds will broaden with the increase of ionic interactions between the alkali- and alkali-earth/rare-earth ions and the $[M_xTe_y]^{z-}$ (M = transition or main metal) framework, for example, γ-$RbBi_3S_5$ (∼1.34 eV) versus $AgBi_3S_5$ (∼0.6 eV),[43] $La_7Sb_9S_{24}$ (∼1.55 eV) versus $La_4FeSb_2S_{10}$ (∼0.9 eV),[44] CdTe (1.44 eV) versus $Cs_2Cd_3Te_4$ (2.48 eV),[34,36] and CdTe (1.44 eV) versus $CsTmCdTe_3$ (2.01 eV).[34] Therefore, a possible way to reduce the band gap of $ARE_2Ag_3Te_5$ is to partially or totally replace A/RE cations with less electropositive metals such as In, Bi, Pb, or Au.

Electronic Structures. The result of band structures and density of states of $CsNd_2Ag_3Te_5$ are shown in Figure 7a. The band structure calculation reveals that both valence band maximum (VBM) and conduction band minimum (CBM) locate at the Γ point, indicating a direct band gap of approximately 1.0 eV for Cs $Nd_2Ag_3Te_5$. This value is consistent with the measured optical band gap (∼0.90 eV). On both sides of the Fermi level, the width of band dispersion between Γ and Z points (or $S \rightarrow R$ and $T \rightarrow Y$) is smaller than 0.2 eV, that is, the slope of band is flat along c^* (c crystallographic axis), which corresponds to large effective mass and slow charge carrier velocity, indicating the possibility of a high Seebeck coefficient but low electrical conductivity,[45] whereas the slope of the band is very steep, about 0.8 eV, along $\Gamma \rightarrow S$ ($R \rightarrow Z$) (i.e., along b^*), which is indicative of fast velocity of charge carriers. This steep band along $\Gamma \rightarrow S$ is related the two-dimensional $^2_\infty[Nd_2Te_5]$ layer and $^2_\infty[Ag_3Te_5]$ layer along [100], indicating that the electrical conductivity along [100] is possibly higher than that in the other two directions, [010] and [001].

The partial density of states (PDOS) of $CsNd_2Ag_3Te_5$ are shown in Figure 7b to illustrate the characteristics of valence bands (VB) and conduction bands (CB) near the Fermi level. The VB of $CsNd_2Ag_3Te_5$ is composed of Ag 4d and Te 5p with minor Nd 5d, whereas the CB is made from Nd 5d and minor Te 5p states. The DOS in the valence band around the Fermi level is large, which may predict a high p-type Seebeck coefficient; however, the DOS in the conduction band around the Fermi level is also very large, which may lead to a high n-type Seebeck coefficient. Therefore, two types of carriers (holes and electrons) may concur, and the positive and negative Seebeck coefficients can be counteracted, which is consistent to the low Seebeck coefficient of the undoped $CsNd_2Ag_3Te_5$ sample in the experiment. Because the CB near the Fermi level is mainly composed of Nd 5d states, we may consider the substitution of Nd by other elements such as In to decrease the DOS in the conduction band around the Fermi level. In fact, we have calculated a hypothetical model in which half of the Nd is

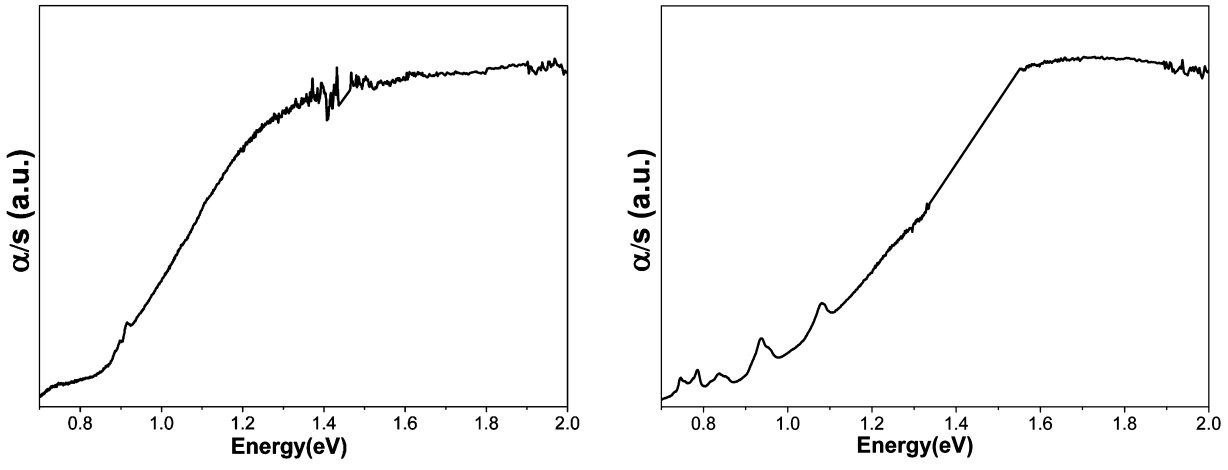

Figure 6. UV−vis diffuse reflectance of (left) $CsNd_2Ag_3Te_5$ and (right) $CsSm_2Ag_3Te_5$.

dx.doi.org/10.1021/ic5007132 | Inorg. Chem. 2014, 53, 6893−6903

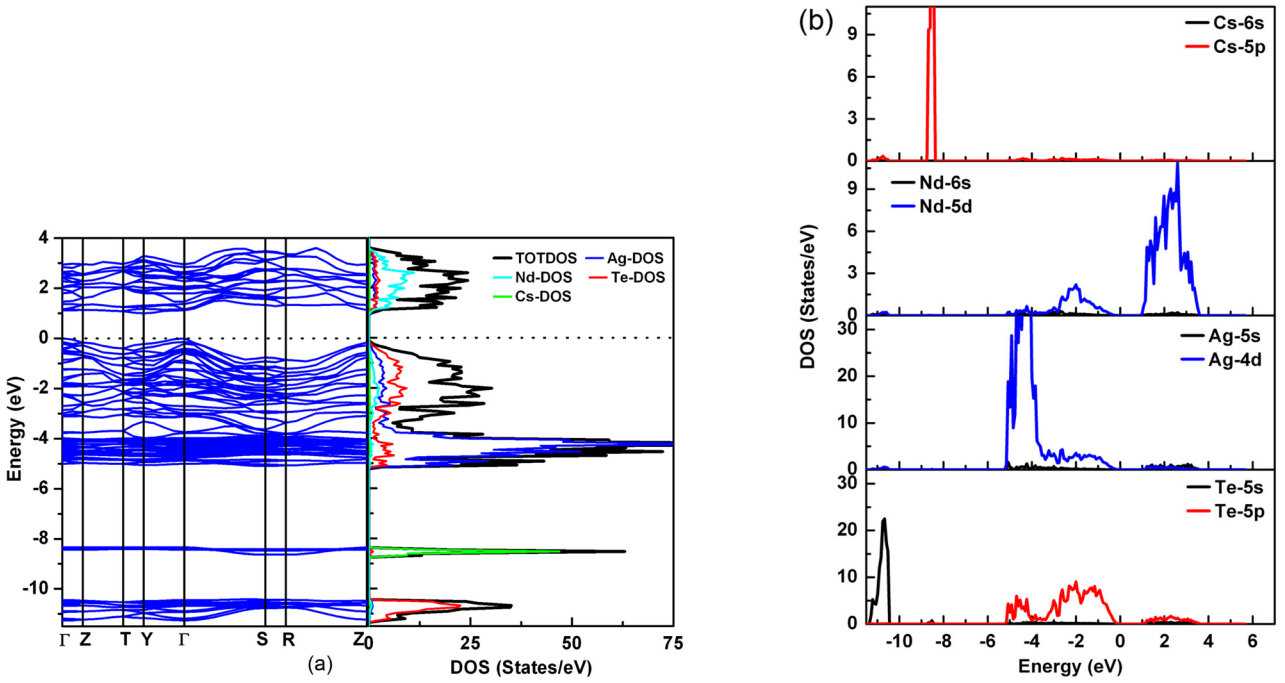

Figure 7. (a) Band structure and density of states of $CsNd_2Ag_3Te_5$ and (b) projected partial density of states (PDOS) of $Cs_2Nd_2Ag_3Te_5$. Fermi level is set to 0 eV.

replaced by In, the result of which shows the DOS in the conduction band around the Fermi level becoming significantly smaller than that in the valence band, and its band structure shows half-metallic character (Figure S1, Support Information). Therefore, it may be possible to optimize thermoelectric properties of $CsRE_2Ag_3Te_5$ (RE = Pr, Nd, Sm, Gd–Er) by carefully selecting the In contents.

Electrical and Thermal Transport Properties. As discussed in the Syntheses section and in $Cs_xRE_2Cu_{6-x}Te_6$,[18] a small amount of CsCl impurity (1.1–1.7%) exists in the pellets, which will have an effect on the TE properties. However, to remove the CsCl impurity or to quantificationally evaluate the influence of such an impurity is impossible under the current experimental conditions. Because the amount of the impurity is not significant, we do not consider the influence to be remarkable. Figure 8 shows the temperature dependence of thermoelectric properties for the undoped sintered polycrystalline pellets of $CsRE_2Ag_3Te_5$. The temperature dependences of specific heat and thermal diffusivity are given in Figures S14 and S15 (Supporting Information). At room temperature, the measured C_p values (Pr, 0.191 J/(g·K); Nd, 0.223 J/(g·K); Sm, 0.192 J/(g·K) and Tb, 0.207 J/(g·K)) are in accordance with the Dulong Petit value (0.198 J/(g·K)).

Figure 8a shows the positive temperature dependence of the electrical conductivity, in accordance with typical semiconducting behavior. These values of the electrical conductivity are lower than those of $Cs_xRE_2Cu_{6-x}Te_6$, $CsBi_4Te_6$[46], and $AeZn_2Sb_2$[7] by 2–3 orders of magnitude (Table 4). The low electrical conductivity is consistent with the relatively large band gap of $CsRE_2Ag_3Te_5$, 0.90 eV (optical)/1.0 eV (calculated). On the other hand, $CsRE_2Ag_3Te_5$ also shows very low thermal conductivity in the entire experimental temperature region in Figure 8c. These values of the thermal conductivity are also significantly lower than those of $Cs_xRE_2Cu_{6-x}Te_6$, $CsBi_4Te_6$, and $Ca_{0.5}Yb_{0.5}Zn_2Sb_2$ listed in Table 4. The carrier contribution to the thermal conductivity (κ_{ele}) was roughly estimated by the Wiedemann–Franz law: $\kappa_{ele} = L\sigma T$, where the Lorenz number (L) = 1.5×10^{-8} W·Ω/K^2.[3,47] The lattice thermal conductivity (κ_{latt}) is predominant in $CsRE_2Ag_3Te_5$; the fraction of the κ_{ele} in the total thermal conductivity is only a few percent. The very low thermal conductivity is likely a consequence of the quaternary heavy constituent elements[46,48] and the larger thermal displacement parameters of Cs and Ag. The heavy atoms give rise to low acoustic phonon frequencies in the materials, and thereby decreases the thermal conductivity. The thermal displacement parameters of Cs and Ag atoms are greater than those of RE and Te by 1.5–2 times, suggesting that Cs and Ag atoms may be playing the role of rattlers and anharmonic vibrations, respectively.[49,50]

The Seebeck coefficient underwent a transition from negative (−49, −7.2, and −30.3 μV/K at 300, 331, and 335 K for Pr-, Nd-, and Sm-samples, respectively) to positive (+18, +27.3, and +28 μV/K at 349, 368, and 376 K for Pr-, Nd-, and Sm-samples, respectively) (Figure 8c), indicating the occurrence of the two-band conduction of electrons and holes for the undoped sintered polycrystalline pellets of $CsRE_2Ag_3Te_5$ (with 1.1, 1.2, 1.3, and 1.7% CsCl impurity for Pr-, Nd-, Sm-, and Tb-samples, respectively). To achieve a high power factor, it is necessary to control one type of carrier transport (electron or holes) because mixed carrier transport (electron and holes) suppresses the Seebeck coefficient.[1] Above 400 K, the Seebeck coefficient rises steadily in a nearly straight line as the temperature increases (Figure 8c) and reaches 163 μV/K at 693 K, 158 μV/K at 712 K, 203 μV/K at 721 K, and 193 μV/K at 686 K for undoped Pr-, Nd-, Sm-, and Tb-samples, respectively, indicating that the main charge carriers are holes at temperatures above 400 K.

The temperature dependence of ZT is calculated and presented in Figure 8d. The ZT value increases with temperature and reaches 0.02 at 693 K, 0.06 at 712 K, 0.04 at 721 K, and 0.04 at 686 K, for undoped Pr-, Nd-, Sm-, and

dx.doi.org/10.1021/ic5007132 | Inorg. Chem. 2014, 53, 6893–6903

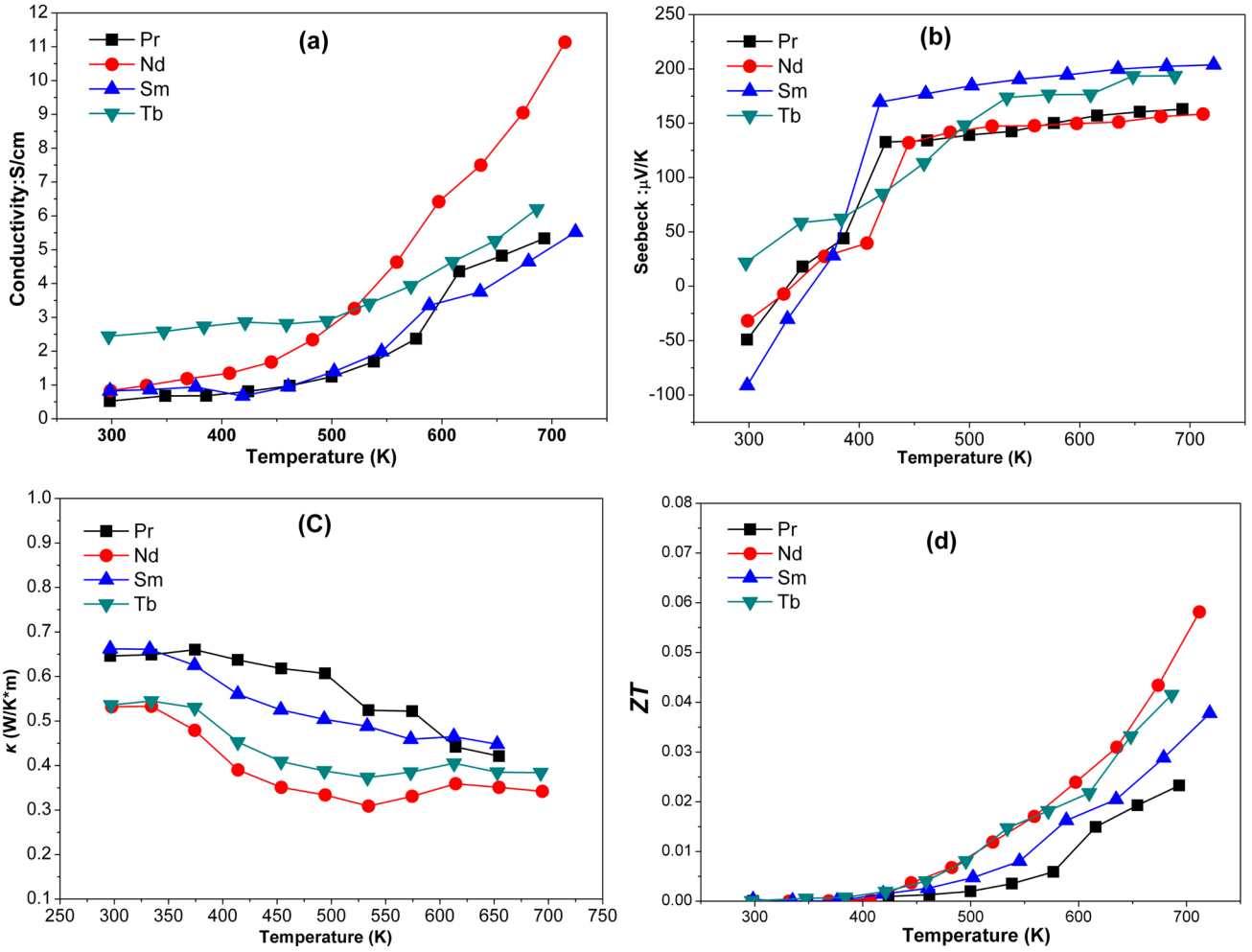

Figure 8. Temperature dependences of (a) electrical conductivity, (b) Seebeck coefficient, (c) total thermal conductivity, and (d) ZT, for undoped sintered polycrystalline $CsRE_2Ag_3Te_5$ pellets. Weight percentage of CsCl impurity is 1.2, 1.1, 1.3, and 1.7% for Pr-, Nd-, Sm-, and Tb-samples, respectively.

Table 4. Thermoelectric Property of $CsRE_2Ag_3Te_5$ (RE = Pr, Nd, Sm, and Tb) Compared to Some Thermoelectric Materials

material	σ (S/cm)	S (μV/K)	κ_{total} (W/(m·K))	ZT	T (K)	ref
$CsPr_2Ag_3Te_5$[a]	0.5	−49	0.65	N/A	300	present work
	5.3	162	0.42	0.02	693	
$CsNd_2Ag_3Te_5$[a]	0.8	−32	0.53	N/A	300	present work
	11	158	0.34	0.06	712	
$CsSm_2Ag_3Te_5$	0.8	−91	0.66	N/A	300	present work
	5.5	204	0.45	0.04	721	
$CsTb_2Ag_3Te_5$[a]	2.4	22	0.54	N/A	300	present work
	6.2	193	0.38	0.04	686	
$Cs_{0.73(2)}Pr_2Cu_{5.27(2)}Te_6$[a]	773	+44	1.66	0.026	300	18
	354	+106	1.14	0.23	660	
$CsBi_4Te_6$[b]	900−450	+90−+150	1.21−1.53	0.18−0.2	300	46
$CaZn_2Sb_2$[c]	422	+120	2.6	0.07	300	7a
$Ca_{0.5}Yb_{0.5}Zn_2Sb_2$[c]	562	+79	1.34	0.08	300	7a
$YbZn_2Sb_2$[c]	3125	+48	4.26	0.05	300	7a

[a]As-synthesized sintered polycrystalline pellet. Weigh percentage of CsCl impurity is 1.2, 1.1, 1.3, 1.7, and 4.2% for Pr-, Nd-, Sm-, Tb- and $Cs_{0.73(2)}Pr_2Cu_{5.27(2)}Te_6$-samples, respectively. [b]Single crystal. [c]Hot-pressed pellet.

Tb-samples, respectively. These values of ZT are too low for practical applications as thermoelectric materials. However, the very low thermal conductivity of $CsRE_2Ag_3Te_5$ leads to a large advantage for thermoelectric applications. The band structure feature discussed above indicates that further optimization of thermoelectric properties is possible via the partial substitution of RE with other elements such as In to decrease the DOS in the conduction band around the Fermi level. For this purpose, we are investigating partial substitutions of RE with other elements like In.

dx.doi.org/10.1021/ic5007132 | Inorg. Chem. 2014, 53, 6893−6903

CONCLUSION

A new series of quaternary $CsRE_2Ag_3Te_5$ (RE = Pr, Nd, Sm, Gd−Er) and $RbRE_2Ag_3Te_5$ (RE = Sm, Gd, Tb, Dy), whose structures are similar to $AeZn_2Sb_2$, with sheets of mixed A^{1+} and RE^{3+} cations between layers of covalently bound Ag−Te, have been synthesized from the elemental mixtures in the ACl flux at 1123 K. The "puckered" layer of $^2_\infty[Ag_3Te_5]$ alternately stacks with the "puckered" layer of $^2_\infty[RE_2Te_5]$ along the *b* axis, forming a 3D mixed covalent and ionic bonding anionic tunnel framework whose tunnels are filled with A. The paramagnetic properties of Pr-, Nd-, and Tb-members obey the Curie−Weiss law. The undoped sintered polycrystalline pellets of $CsRE_2Ag_3Te_5$ (containing 1.1−1.7% CsCl impurity) show very low electrical conductivity, very low thermal conductivity, and the occurrence of the two-band conduction of electrons and holes, obtaining ZTs of 0.02 at 693 K, 0.06 at 712 K, 0.04 at 721 K, and 0.04 at 686 K for undoped Pr-, Nd-, Sm-, and Tb-samples, respectively. The electrical conductivity, Seebeck coefficients, and optical band gap measurements, as well as the theoretical calculations, show that the title compounds are typical semiconductors.

ASSOCIATED CONTENT

Supporting Information

Additional tables containing crystallographic data, XRD patterns, density of states of hypothetical $CsInNdAg_3Te_5$, and cif data. This material is available free of charge via the Internet at http://pubs.acs.org.

AUTHOR INFORMATION

Corresponding Author

*E-mail: mengchyu_2007@163.com. Tel: (+86) 775-2661766.

Notes

The authors declare no competing financial interest.

ACKNOWLEDGMENTS

This research was supported by the National Natural Science Foundation of China (Grant Nos. 90922021, 20973175, 51362030), the Knowledge Innovation Program of the Chinese Academy of Sciences (Grant No. KJCX2-YW-H20), and the GuangXi Natural Science Foundation of China (Grant No. 2013GXNSFBA019047).

REFERENCES

(1) Rowe, D. M., Ed. *CRC Handbook of Thermoelectrics*; CRC Press: Boca Raton, FL, 1995.
(2) Qiu, P. F.; Yang, J.; Liu, R. H.; Shi, X.; Huang, X. Y.; Snyder, G. J.; Zhang, W.; Chen, L. D. *J. Appl. Phys.* **2011**, *109*, 063713.
(3) Shi, X.; Yang, J.; Salvador, J. R.; Chi, M. F.; Cho, J. Y.; Wang, H.; Bai, S. Q.; Yang, J. H.; Zhang, W. Q.; Chen, L. D. *J. Am. Chem. Soc.* **2011**, *133*, 7837−7846.
(4) Caillat, T.; Borshchevsky, A.; Fleurial, J. P. *J. Appl. Phys.* **1996**, *80*, 4442−4449.
(5) Chung, D. Y.; Hogan, T.; Brazis, P.; Rocci-Lane, M.; Kannewurf, C.; Bastea, M.; Uher, C.; Kanatzidis, M. G. *Science* **2000**, *287*, 1024−1027.
(6) Toberer, E. S.; Christensen, M.; Iversen, B. B.; Snyder, G. J. *Phys. Rev. B* **2008**, *77*, 075203−1−8.
(7) (a) Gascoin, F.; Ottensmann, S.; Stark, D.; Haile, S. M.; Snyder, G. J. *Adv. Funct. Mater.* **2005**, *15*, 1860−1864. (b) Zhang, H.; Zhao, J. T.; Grin, Y.; Wang, X. J.; Tang, M. B.; Man, Z. Y.; Chen, H. H.; Yang, X. X. *J. Chem. Phys.* **2008**, *129*, 164713. (c) Toberer, E. S.; May, A. F.; Melot, B. C.; Flage-Larsen, E.; Snyder, G. J. *Dalton Trans.* **2010**, *39*, 1046−1054.
(8) Toberer, E. S.; May, A. F.; Snyder, G. J. *Chem. Mater.* **2010**, *22*, 624−634.
(9) Snyder, G. J.; Toberer, E. S. *Nat. Mater.* **2008**, *7*, 105−114.
(10) Kauzlarich, S. M.; Brown, S. R.; Snyder, G. J. *Dalton Trans.* **2007**, *21*, 2099−2107.
(11) Huang, F. Q.; Choe, W.; Lee, S.; Chu, J. S. *Chem. Mater.* **1998**, *10*, 1320−1326.
(12) Babo, J. M.; Schleid, T. *Solid State Sci.* **2010**, *12*, 238−245.
(13) Babo, J. M.; Strobel, S.; Schleid, T. *Z. Anorg. Allg. Chem.* **2010**, *636*, 349−355.
(14) (a) Babo, J. M.; Choi, E. S.; Albrecht-Schmitt, T. E. *Inorg. Chem.* **2012**, *51*, 11730−11735. (b) Patschke, R.; Heising, J.; Kanatzidis, M.; Brazis, P.; Kannewurf, C. R. *Chem. Mater.* **1998**, *10*, 695−697.
(15) Patschke, R.; Brazis, P.; Kannewurf, C. R.; Kanatzidis, M. G. *J. Mater. Chem.* **1999**, *9*, 2293−2296.
(16) Patschke, R.; Brazis, P.; Kannewurf, C. R.; Kanatzidis, M. *J. Mater. Chem.* **1998**, *8*, 2587−2589.
(17) Patschke, R.; Brazis, P.; Kannewurf, C. R.; Kanatzidis, M. *Inorg. Chem.* **1998**, *37*, 6562−6563.
(18) Meng, C. Y.; Chen, H.; Wang, P.; Chen, L. *Chem. Mater.* **2011**, *23*, 4910−4919.
(19) Johnsen, S.; Peter, S. C.; Nguyen, S. L.; Song, J. H.; Jin, H.; Freeman, A. J.; Kanatzidis, M. G. *Chem. Mater.* **2011**, *23*, 4375−4383.
(20) Seifert, H. J. *J. Therm. Anal. Calorim.* **2002**, *67*, 789−826.
(21) Roffe, M.; Seifert, H. J. *J. Alloys Compd.* **1997**, *257*, 128−133.
(22) Reuter, G.; Sebastian, J.; Roffe, M.; Seifert, H. J. *Thermochim. Acta* **1997**, *296*, 47−52.
(23) Reuter, G.; Frenzen, G. *J. Solid State Chem.* **1995**, *116*, 329−334.
(24) Mitra, S.; Uebach, J.; Seifert, H. J. *J. Solid State Chem.* **1995**, *115*, 484−489.
(25) *CrystalClear*, version 1.3.5; Rigaku Corp.: The Woodlands, TX, 1999.
(26) Sheldrick, G. M. *SHELXTL*, version 5.1; Bruker AXS: Madison, WI, 1998.
(27) Kortüm, G. *Reflectance Spectroscopy. Principles, Methods, Applications.*; Springer: New York, 1969.
(28) Kresse, G.; Furthmuller, J. *Comput. Mater. Sci.* **1996**, *6*, 15−50.
(29) Perdew, J. P.; Wang, Y. *Phys. Rev. B* **1992**, *45*, 13244−13249.
(30) Kresse, G.; Joubert, D. *Phys. Rev. B* **1999**, *59*, 1758−1775.
(31) Blochl, P. E. *Phys. Rev. B* **1994**, *50*, 17953−17979.
(32) Huang, F. Q.; Ibers, J. A. *J. Solid State Chem.* **2000**, *151*, 317−322.
(33) Yao, J. Y.; Deng, B.; Sherry, L. J.; McFarland, A. D.; Ellis, D. E.; Van Duyne, R. P.; Ibers, J. A. *Inorg. Chem.* **2004**, *43*, 7735−7740.
(34) Liu, Y.; Chen, L.; Wu, L. M. *Inorg. Chem.* **2008**, *47*, 855−862.
(35) Huang, F. Q.; Brazis, P.; Kannewurf, C. R.; Ibers, J. A. *J. Am. Chem. Soc.* **2000**, *122*, 80−86.
(36) Narducci, A. A.; Ibers, J. A. *J. Alloys Compd.* **2000**, *306*, 170−174.
(37) Zhang, X.; Park, Y. B.; Hogan, T.; Schindler, J. L.; Kannewurf, C. R.; Seong, S.; Albright, T.; Kanatzidis, M. G. *J. Am. Chem. Soc.* **1995**, *117*, 10300−10310.
(38) O'Connor, C. *J. Prog. Inorg. Chem.* **1982**, *29*, 203−283.
(39) West, A. R. *Solid State Chemistry and Its Applications*; John Wiley &Sons: Chichester, U.K., 1984.
(40) Mitchell, K.; Huang, F. Q.; McFarland, A. D.; Haynes, C. L.; Somers, R. C.; Van Duyne, R. P.; Ibers, J. A. *Inorg. Chem.* **2003**, *42*, 4109−4116.
(41) Mitchell, K.; Haynes, C. L.; McFarland, A. D.; Van Duyne, R. P.; Ibers, J. A. *Inorg. Chem.* **2002**, *41*, 1199−1204.
(42) Kahn, O. *Molecular Magnetism*; VCH Publishers: New York, 1993.
(43) Kim, J. H.; Chung, D. Y.; Bilc, D.; Loo, S.; Short, J.; Mahanti, S. D.; Hogan, T.; Kanatzidis, M. G. *Chem. Mater.* **2005**, *17*, 3606−3614.
(44) Zhao, H. J.; Li, L. H.; Wu, L. M.; Chen, L. *Inorg. Chem.* **2009**, *48*, 11518−11524.
(45) Snyder, G. J.; Toberer, E. S. *Nat. Mater.* **2008**, *7*, 105−114.

(46) Chung, D. Y.; Hogan, T. P.; Rocci-Lane, M.; Brazis, P.; Ireland, J. R.; Kannewurf, C. R.; Bastea, M.; Uher, C.; Kanatzidis, M. G. *J. Am. Chem. Soc.* **2004**, *126*, 6414−6428.
(47) Kittel, C. *Introduction to Solid State Physics*, 7th ed.; John Wiley & Sons: New York, 1996.
(48) Majumdar, A. *Science* **2004**, *303*, 777−778.
(49) Young, D. P.; Brown, C. L.; Khalifah, P.; Cava, R. J.; Ramirez, A. P. *J. Appl. Phys.* **2000**, *88*, 5221−5224.
(50) Sales, B. C.; Chakoumakos, B. C.; Mandrus, D.; Sharp, J. W. *J. Solid State Chem.* **1999**, *146*, 528−532.

dx.doi.org/10.1021/ic5007132 | *Inorg. Chem.* 2014, 53, 6893−6903